

Cite this: *Mater. Horiz.*, 2020,
7, 843Received 28th August 2019,
Accepted 25th November 2019

DOI: 10.1039/c9mh01367a

rsc.li/materials-horizons

Mapping mechanisms and growth regimes of magnesium electrodeposition at high current densities†

Rachel Davidson,^{ab} Ankit Verma,^{id} c David Santos,^{ab} Feng Hao,^{id} c Cole D. Fincher,^d Dexin Zhao,^b Vahid Attari,^{bd} Parker Schofield,^{ab} Jonathan Van Buskirk,^{id} ab Antonio Fraticelli-Cartagena,^a Theodore E. G. Alivio,^{ab} Raymundo Arroyave,^{bd} Kelvin Xie,^b Matt Pharr,^d Partha P. Mukherjee ^{id} *c and Sarbajit Banerjee ^{id} *ab

The utilization of metallic anodes holds promise for unlocking high gravimetric and volumetric energy densities and is pivotal to the adoption of 'beyond Li' battery chemistries. Much of the promise of magnesium batteries stems from claims regarding their lower predilection for dendrite growth. Whilst considerable effort has been invested in the design of novel electrolytes and cathodes, detailed studies of Mg plating are scarce. Using galvanostatic electrodeposition of metallic Mg from Grignard reagents in symmetric Mg–Mg cells, we establish a phase map characterized by disparate morphologies spanning the range from fractal aggregates of 2D nanoplatelets to highly anisotropic dendrites with singular growth fronts and nanowires entangled in the form of mats. The effects of electrolyte concentration, applied current density, and coordinating ligands have been explored. The study demonstrates a complex range of electrodeposited morphologies including canonical dendrites with shear moduli conducive to penetration through typical polymeric separators. We further demonstrate a strategy for mitigating Mg dendrite formation based on the addition of molecular Lewis bases that promote nanowire growth through selective surface coordination.

New concepts

Here, we explore electrodeposition of magnesium under varying electric fields, electrolyte concentrations, and added ligands. Distinctive growth mechanisms are differentiated including fractal and dendritic growth regimes, which are rationalized based on the dynamical interplay between electrochemical reaction and self-diffusion rates. Limitations of current batteries represent perhaps the largest roadblock to the continued advancement of renewable energy technologies. Supplanting the graphite used in Li-ion batteries with metallic anodes holds promise for significantly enhanced capacity and energy density but requires mitigating the proclivity of lithium to deposit as dendrites. The 'beyond Li' paradigm of energy storage has attracted consideration attention with much of its promise derived from the utilization of metallic anodes that are safer in comparison to lithium. The manuscript presents characterization of electrodeposition products across multiple length scales. We note unprecedented single crystal growth of Mg dendrites, which has not heretofore been reported and has no parallels in the lithium dendrite literature. Mg dendrites are found to be substantially harder than their lithium counterparts, which further underscores the need for stiffer separators. The addition of dodecanethiol alters growth dynamics leading to consistent isolation of nanowires and mitigation of dendritic growth.

Introduction

Lithium-ion batteries are currently the dominant electrochemical energy storage technology with accessible gravimetric and

volumetric energy densities approaching 250 W h kg⁻¹ and 600 W h L⁻¹, respectively.^{1,2} Current Li-ion batteries pair transition metal oxide cathodes with graphite anodes;³ supplanting the latter with metallic lithium would yield theoretical capacities as

^a Department of Chemistry, Texas A&M University, College Station, TX 77843, USA. E-mail: banerjee@chem.tamu.edu

^b Department of Materials Science & Engineering, Texas A&M University, College Station, TX 77843, USA

^c School of Mechanical Engineering, Purdue University, West Lafayette, IN 47907, USA. E-mail: pmukherjee@purdue.edu

^d Department of Mechanical Engineering, Texas A&M University, College Station, TX 77843, USA

† Electronic supplementary information (ESI) available: Videos: S1. Time lapse video of growth from 0.921 mA cm⁻² in 0.25 M MeMgCl solution for 24 h reactions shown at 4000× speed. S2. Time lapse video of growth from 0.921 mA cm⁻² in 0.5 M MeMgCl solution for 24 h reactions shown at 4000× speed. S3. Time lapse video of growth from 0.921 mA cm⁻² in 1.0 M MeMgCl solution for 24 h reactions shown at 4000× speed. S4. Time lapse video of growth from 0.921 mA cm⁻² in 1.5 M MeMgCl solution for 24 h reactions shown at 4000× speed. S5. Time lapse video of growth from 0.921 mA cm⁻² in 2.0 M MeMgCl solution for 24 h reactions shown at 4000× speed. S6. Time lapse video of growth from 0.921 mA cm⁻² in 0.5 M MeMgCl solution with addition of 0.0626 M dodecanethiol for 24 h reactions shown at 4000× speed. S7. Time lapse video of growth from 0.921 mA cm⁻² in 0.5 M MeMgCl solution with addition of 0.125 M dodecanethiol for 24 h reactions shown at 4000× speed. S8. Time lapse video of growth from 0.921 mA cm⁻² in 0.5 M MeMgCl solution with addition of 0.188 M dodecanethiol for 24 h reactions shown at 4000× speed. S9. The alighted tilt series of soft X-ray microscopy images of a fractal grown at 0.921 mA cm⁻² in 0.5 M MeMgCl for 24 h obtained at the Mg K-edge in transmission (left) and optical density (right). S10. 3D reconstruction series of soft X-ray microscopy images of a fractal grown at 0.921 mA cm⁻² in 0.5 M MeMgCl for 24 h obtained at the Mg K-edge in transmission (left) and optical density (right). S11. 3D digital tomography of growth from 0.921 mA cm⁻² in 0.5 M MeMgCl solution for 24 h reactions. S12. 3D digital tomography of growth from 0.921 mA cm⁻² in 2.0 M MeMgCl solution for 24 h reactions. See DOI: 10.1039/c9mh01367a

high as 3860 mA h g^{-1} .⁴ However, Li metal has a high propensity for dendrite formation; the plating of lithium as anisotropic fractal structures that can bridge across liquid and solid electrolytes, thereby short-circuiting the cell, represents a major safety hazard. Consequently, the paucity of scalable methods to achieve reproducible electroplating of metallic lithium has emerged as a substantial roadblock to accessing improved storage capacities.^{5,6} Dendrite formation has been the scourge even when utilizing graphite anodes wherein under specific temperature, voltage, and electrolyte decomposition conditions, dendritic growth regimes become more favourable as compared to insertion reactions. Indeed, numerous high-profile incidents have underscored the importance of understanding the accumulative impact of low-probability, stochastic processes in electrochemical energy storage systems wherein fundamental processes operate across multiple decades of time and length scales. Developing experimental conditions that replicate such local far-from-equilibrium behaviour has thus emerged as an urgent imperative. Considerable effort has been invested in the development of “beyond Li” intercalation systems that derive a considerable portion of their promise from the potential to utilize their respective metallic anodes. Sodium, magnesium, calcium, and zinc are considered to deposit with much lower propensities for dendrite formation as compared to lithium owing to their more facile self-diffusion, which thereby results in the plating of relatively homogeneous deposits.^{7–9}

Magnesium batteries are considered a promising alternative given the divalent charge of Mg, which has been proposed as a means of achieving higher energy densities since most cathode materials are limited in terms of their available redox sites and not accessible redox states. In addition, magnesium holds promise for enabling use of metal anodes as a result of its supposed “non-dendrite” forming nature.^{10–14} Groß has attributed the low propensity for dendrite formation to small self-diffusion barriers and vanishingly small Ehrlich–Schwöbel barriers for 3D diffusion. Much research has targeted the development of novel cathode materials that can readily diffuse highly polarizing divalent Mg-ions as well as in the development of electrolytes stable across extended potential windows that allow for effective desolvation of magnesium at electrode interfaces.^{12,15–20} Ideas regarding the permeability or lack thereof of divalent Mg-ions through solid electrolyte interfaces (SEI), which may form through degradation of electrolytes during cycling, have inspired the design of several stable classes of electrolytes.^{12,21–23}

Several experimental observations of homogeneous plating as compared to agglomerate formation support the idea of a reduced predilection of magnesium towards formation of dendritic structures.^{10,13,14,24–26} Dual-salt electrolytes containing both Li and Mg components have been considered as a means of utilizing the faster kinetics of Li at the cathode whilst avoiding Li dendrite formation through preferential plating of Mg at the anode.^{27,28} The faster surface diffusion of Mg-ions along the Mg(0001) plane predicted from first-principles calculations has been put forth as the intrinsic basis for reduced propensity for dendritic growth and is further corroborated by

the prediction of low diffusion barriers for diffusion across steps and terraces.⁷ Self-diffusion coefficients, Ehrlich–Schwöbel barriers, and anisotropy resulting from the intrinsic crystal structure have emerged as some putative descriptors for comparing the dendrite-forming nature of different anode materials.^{26,29–32} While reports of reduced propensity for dendrite growth in magnesium are well founded, it is worth noting that electrodeposition processes often occur far from equilibrium wherein otherwise reliable descriptors can be thwarted by other vectors.³³ Inhomogeneities in magnesium deposition are not unprecedented^{34–36} and capacity fading analogous to the problems discussed with lithium has been observed.^{37,38} Recently Bitenc and co-workers showed highly uneven deposition in $\text{MgCl}_2\text{-AlCl}_3\text{-DME}$ electrolyte systems.³⁶ Groß and co-workers have pointed out that surface self-diffusion in itself cannot explain the deposition characteristics; the applied current density is an equally important measure, which determines the incoming reactant flux.^{39–41} Yet, comprehensive investigations of non-equilibrium phase spaces and Mg electrometallurgy are scarce even though reports of fractal Mg microstructures within alloys are abundant in the metallurgy literature.^{42,43}

Fractal and dendritic magnesium deposits have indeed been observed upon the electrodeposition of Grignard reagents¹² in Mg–Mg symmetric cells monitored *in situ* with videomicroscopy under galvanostatic conditions. In this article, overpotentials required for electrocrystallization of Mg at varying concentrations and current densities are explored, and distinctive growth morphologies are delineated including unambiguous fractal and dendritic growth regimes. Deposition is seen to be underpinned by diffusion-limited aggregation (DLA) mechanisms across much of the examined reaction space.^{6,44–51} The Mg deposits have been extensively explored across different length scales utilizing a combination of electron and X-ray microscopy. The experimental observations are explained with reference to an analytical framework contrasting the Mg^{2+} diffusive transport and reaction rates wherein exacerbated electrodeposition instabilities are anticipated beyond the “Sand’s time” limit at elevated current densities.⁵² Furthermore, phase-field modeling studies have been used to unravel the mechanistic underpinnings of the observed electrodeposited morphologies.

Results and discussion

Formation and characterization of fractal Mg structures: developing a phenomenological map of deposition regimes

Electrodeposition of metallic Mg from MeMgCl and EtMgCl in tetrahydrofuran (THF) has previously been shown to yield continuous thin film and nanowire array morphologies; the latter has been proposed to result from a modified faces, steps, and kinks mechanism governed primarily by the deposition rate.⁵³ While these electrolytes have limited stability windows, they have been extensively used for Mg electrodeposition and serve as effective model systems as compared to multicomponent electrolytes. The utilization of a symmetric cell geometry to examine electrocrystallization of Mg as will be discussed here mitigates the influence of convoluting factors such as insertion

reactions, electrolyte decomposition at the cathode, and dissolution of the cathode as a result of parasitic reactions. The use of Mg ribbon electrodes further allows for direct observation of intrinsic phenomena without potential confounding factors such as electrocatalytic processes at transition metal electrodes. Nevertheless, similar results are obtained for Pt, stainless steel, A36 steel, and galvanized steel. Application of a voltage in a parallel-plate geometry yields a variety of morphologies of Mg spanning the range from aggregated polycrystalline quasi-spherical deposits to dendrites spanning millimeters in length, aggregated platelets, and nanowires, depending on the current density, concentration, and presence of coordinating ligands (*vide infra*). Videos S1–S8 (ESI[†]) illustrate time-lapse images of Mg deposition as a function of varying concentration of MeMgCl (Videos S1–S5, ESI[†]) and concentration of added dodecanethiol (Videos S6–S8, ESI[†]).

Fig. 1A shows a phenomenological map illustrating the different observed growth regimes for electroplating of Mg, indicating considerable complexity as well as clear dendritic growth windows in the multidimensional space. The plot charts out correlations between processing conditions and mesoscale texture and microstructure evolving from the interplay between thermodynamics and kinetics of Mg electrodeposition. Intriguingly, this richness of electrodeposited Mg morphologies does not appear to have been previously reported in the literature even for these common electrolytes. Generally, upon increase in concentration of the electrolyte, an increase in the grain size of the deposit is observed resulting in a transition from highly

fractal growths formed from aggregation of hexagonal platelets to aggregates of quasi-spherical deposits and finally converging towards stabilization of highly crystalline dendritic deposits with singular dominant growth fronts. Such morphologies represent anisotropic growth regimes, which could detrimentally impact battery performance; mapping such mechanisms is imperative in order to systematically tune the nature of electrodeposited films and to enable identification of consistent, controllable, and stable plating windows. Fig. 1 depicts, as will be discussed below, that the inclusion of dodecanethiol yields nanowire morphologies in the form of mats, which may offer a route to the design of cyclable high-surface-area metal anodes. In the sections below, we will discuss this phase space across multiple length scales while delineating observations from monitoring the evolution of mesoscale morphologies, resulting microstructure, and crystal structure for each distinctive regime.

Mesoscale and higher length scale plating morphologies have been monitored using videomicroscopy (Videos S1–S8, ESI[†]). Fig. 1B depicts a typical fractal deposit formed from the electrodeposition of Mg from a 0.5 M solution of MeMgCl in THF at a constant current density of 0.921 mA cm⁻². The deposits span several millimeters in length, are highly branched, and grow from the edges of the Mg ribbon. Fig. 1C shows a SEM image of the same deposits depicted in Fig. 1B. SEM images of the fractal deposits indicate aggregates of hexagonal platelets characteristic of the intrinsic habit of hcp Mg. Crystallographic information has further been derived from high-resolution TEM and XRD in order to understand the electrocrystallization process.

Powder XRD patterns of all deposits exhibits sharp reflections that can be readily indexed to PDF 35-0821, corresponding to metallic magnesium as is shown in Fig. 1D for the fractal and dendritic deposits. XPS spectra have further been acquired for fractal deposits to examine the elemental composition of their surfaces. Samples were exposed briefly to ambient environments during loading of the substrates within the instrument. Fig. S1A (ESI[†]) shows a survey scan, whereas high-resolution scans for Mg 2p, O 1s, C 1s, and Cl 2p are shown in Fig. 1SB–E (ESI[†]), respectively. The Mg 2p high-resolution XPS spectrum exhibits the presence of zero-valent Mg at 49.5 eV. Some samples additionally show a smaller second peak at 52.6 eV, which can be ascribed to surficial Mg–Cl known to exist as a key passivating species in the electrodeposition of Grignard reagents,⁵⁴ as well as a feature centered at 55.9 eV arising from the Fe 3p spectrum of impurities resulting from the steel electrode clips. As the clips were not submerged in solution during the reaction, the influence of Fe on the characteristics of deposits was considered to be negligible and is an artifact of washing the electrodes following the reaction (the Fe signal is not observed in samples where just the electrodes are washed). The oxygen 1s XPS spectrum shows a prominent peak centered at 531.4 eV, which can be assigned to Mg(OH)₂. A weak shoulder at 529.9 eV is additionally observed likely arising from MgO and at 533.5 eV ascribed to the presence of surface-bound ether species given the strong complexation of THF and ethers to magnesium.^{55,56} High resolution

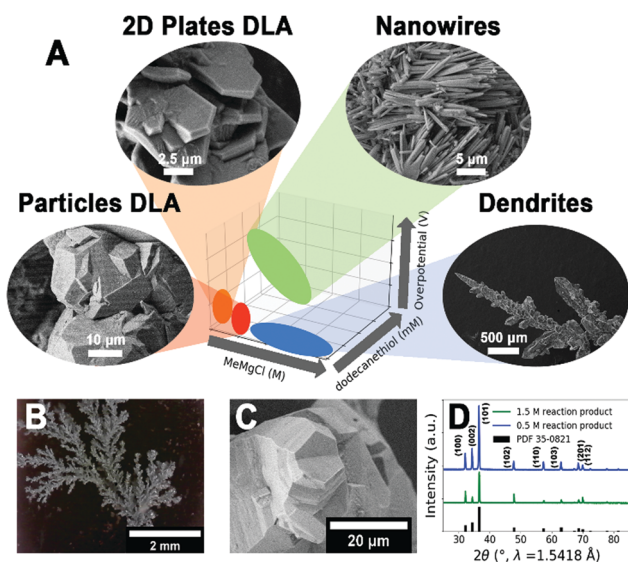


Fig. 1 Fractal growth of electrodeposited Mg. (A) Phenomenological map depicting several differentiated growth regimes as a function of reaction variables. 2D diffusion-limited-aggregation-type growth, regions with spherical diffusion-limited aggregation growth, dendritic growth, and nanowire growth are distinguishable across this parameter space. Characterization of Mg deposits obtained at a constant current density of 0.921 mA cm⁻² from a 0.5 M solution of MeMgCl in THF. (B) Digital photograph of a magnesium fractal deposit; (C) SEM image showing a high-magnification view of the fractal surface; clear hexagonal habits can be discerned. (D) Powder XRD patterns acquired for detached Mg deposits grown from 0.5 and 1.5 M MeMgCl in THF.

scans of the C 1s region show adventitious carbon as well as smaller peaks at 288.2 eV and 289.4 eV, which can be assigned to carboxylates and carbonates, respectively.⁵⁷

Fig. S2A–C (ESI[†]) indicate projections of 3D tomography maps constructed using soft-X-ray microscopy at the Mg K-edge. Videos S9 and S10 (ESI[†]) show the resulting aligned tilt series and the 3D reconstruction, respectively, in terms of the transmission intensity (left) and optical density (right). The fractal aggregate structures are observed to be solid with faceted surfaces.

In situ observations of dendrite growth under varying deposition conditions

Studies of fractal growth in metallic copper and zinc deposits have shown that various experimental parameters affecting the reactivity or diffusion of the electrolyte allow for tuning of the crystallinity as well as the compactness of the plated deposits.^{58–61} Bazant noted that considerations such as the anisotropy of crystal structures or the high activity of light

metals add complexity but do not fundamentally alter the influence of these parameters.⁴⁸ Magnesium electrodeposition from Grignard's agents in THF solution has been first monitored as a function of the applied current density for an overall duration of 8 h from 0.5 M THF solutions of MeMgCl. Digital photographs indicating the formation of fractal structures at 2, 4, 6, and 8 h time points are depicted in Fig. 2. Increasing the current density increases the extent of deposition and yields more heavily branched deposits. This observation as well as the lack of extended crystalline order within the deposits suggests the operation of a diffusion-limited aggregation (DLA) mechanism, as has been observed for dendritic lithium growth.^{48,62} Higher certainty of reduction of metal ions at a given site (oftentimes quantified using a "sticking coefficient",^{63,64}) resulting from the increased driving force for deposition at higher current densities results in more extensive fractal growth. The flux and reaction rates under these conditions overcome the relatively fast self-diffusion predicted for Mg.⁷ Table 1 shows the resulting weights of the fractal product and overpotentials required to maintain the constant current conditions. Generally, there is an increase in the overpotential with increasing current density; the resulting mass of fractal deposits is furthermore increased. The analytically predicted total Mg deposition is also tabulated as anticipated from Faraday's law; detailed analysis is presented in the latter half of this article. The conditions correspond to relatively high current densities, but it is worth noting that proposed fast charging applications will indeed necessitate high current fluxes. Corresponding voltage over time plots are shown in Fig. S3 (ESI[†]).

The growth regimes have been additionally monitored as a function of electrolyte concentration. Time lapse digital photographs acquired at 6, 8, 12, and 16 h intervals are shown in Fig. 3 for different electrolyte concentrations in THF. Videos exhibiting the progression of dendrite growth as a function of time are shown in Videos S1–S5 (ESI[†]) and the characteristics of the deposited products are noted in Table 1. Corresponding voltage *versus* time plots are shown in Fig. S4 (ESI[†]). Increasing

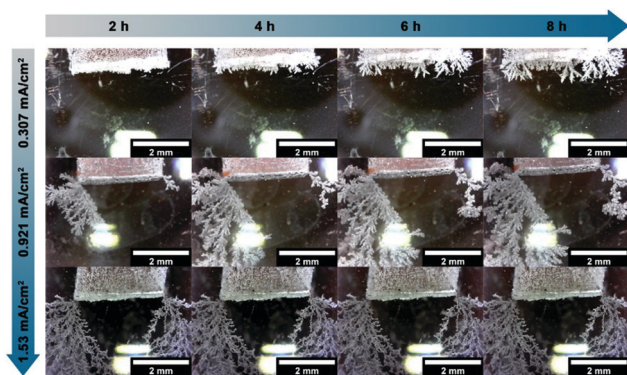


Fig. 2 *In situ* videomicroscopy observations of fractal growth as a function of applied current density. Digital photographs have been acquired at 2, 4, 6, and 8 h time points for deposition from 0.5 M THF solutions of MeMgCl solutions under different applied current densities (0.307, 0.921, and 1.54 mA cm⁻²).

Table 1 Mass of dendritic product and overpotential as a function of applied current density and concentration of MeMgCl. Depositions with varying current density were performed for 8 h and in 0.5 M MeMgCl solutions. Reactions with varying electrolyte concentration were performed for 24 h at an applied current density of 0.921 mA cm⁻²

Variation of applied current density					
Current density (mA cm ⁻²)	Predicted total deposition mass of Mg (mg)	Measured mass of dendritic Mg (mg)	<i>V h</i>	Volts (average)	<i>E</i> (V mm ⁻¹)
0.307	3.63	6.8 ± 0.2	100.7	12.6	0.220
0.921	10.9	6.2 ± 1.3	158.7	19.8	0.347
1.54	18.1	14.2 ± 5.0	222.7	27.8	0.487
Variation of electrolyte concentration					
MeMgCl concentration (M)	Predicted total deposition mass of Mg (mg)	Measured mass of dendritic Mg (mg)	<i>V h</i>	Volts (average)	<i>E</i> (V mm ⁻¹)
0.25	32.64	21.6 ± 9.0	568.0	23.7	0.414
0.50	32.64	27.8 ± 14.3	466.3	19.4	0.340
1.0	32.64	9.1 ± 1.6	37.7	1.6	0.027
1.5	32.64	13.9 ± 3.9	10.3	0.4	0.008
2.0	32.64	12.1 ± 6.8	7.0	0.3	0.005

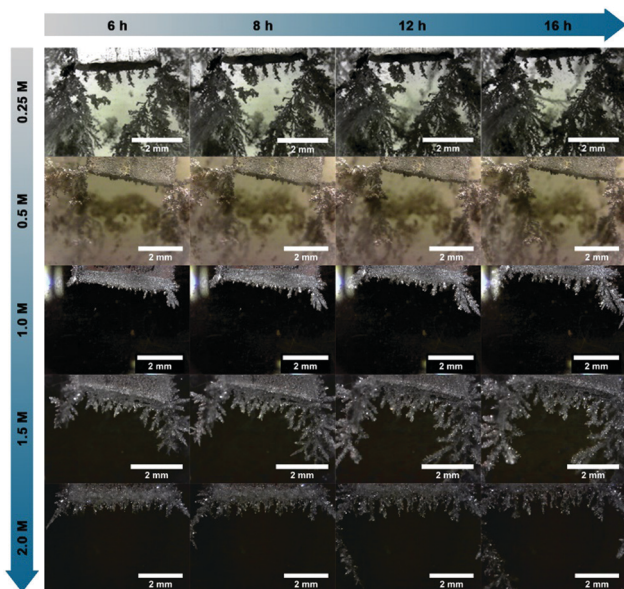


Fig. 3 *In situ* videomicroscopy observations of fractal growth as a function of electrolyte concentration. Digital images acquired at 6, 8, 12, and 16 h time intervals for 0.25, 0.5, 1, 1.5, and 2.0 M concentrations of MeMgCl in THF at a constant current density of 0.921 mA cm^{-2} .

MeMgCl concentration results in the formation of thicker, less branched deposits, which is thought to be reflective of modification in the growth mechanism. In addition, the microstructure of the deposits is modified upon going from 0.25 to 0.5 M with the 0.25 M reactions yielding fractals constituted from much smaller grains as can be seen more clearly in Fig. 4. The overpotential generally decreases with increasing concentration for all samples as a result of the higher solution conductivity. Typically, electrolyte ionic conductivity exhibits a non-monotonic trend with concentration, increasing until an optimal concentration is reached,

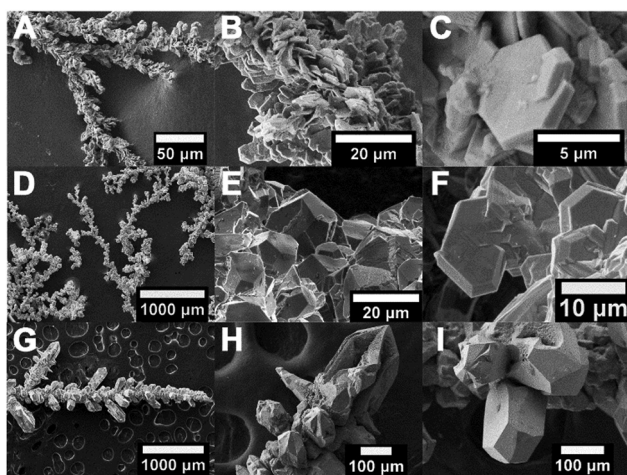


Fig. 4 Fractal to dendrite transformation. SEM images acquired at varying magnifications for deposits obtained at a constant current density of 0.921 mA cm^{-2} for (A–C) 0.25 M; (D–F) 0.5 M; and (G–I) 1.5 M solutions of MeMgCl in THF. The top two rows exhibit fractal growth, whereas the bottom row corresponds to a dendritic growth regime.

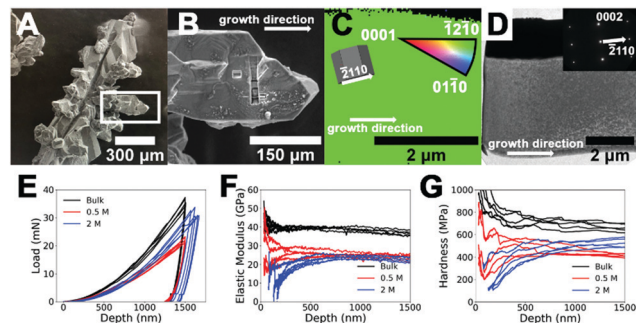


Fig. 5 Microstructural characterization of Mg dendrites. (A) SEM image of a Mg dendrite electrodeposited under 0.921 mA cm^{-2} applied constant current in a 1.5 M MeMgCl for 24 h; (B) higher magnification SEM image of (A) illustrating regions from which EBSD and TEM specimens have been extracted using FIB; (C) EBSD IPF map and 3D crystallographic schematic of the Mg dendrite; (D) bright-field TEM image of the Mg dendrite and corresponding SAED pattern. Representative nanoindentation (E) load-depth curves, (F) elastic modulus versus depth, and (G) hardness versus depth for Mg electrodeposits grown from 0.5 M and 2 M MeMgCl solutions under 0.921 mA cm^{-2} applied constant current for 24 h.

beyond which it is diminished.⁶⁵ For MeMgCl in THF, a steady decrease in overpotential is observed even up to concentrations of 2 M.

The morphologies observed upon non-equilibrium, fractal growth are governed by a balance between local surface dynamics, long-range diffusion, nucleation probabilities, and anisotropic growth rates along different crystallographic directions.⁶⁶ Fig. 4 shows SEM images acquired at different magnifications for deposits obtained from 0.25, 0.5, and 1.5 M solutions of MeMgCl in THF (at a constant current density of 0.921 mA cm^{-2}), which allow for different types of microstructures constituting the fractal morphologies to be differentiated. Fig. 5 shows more extensive crystallographic and nanomechanical characterization of the deposits.

Three distinctive growth regimes can be distinguished with considerable differences in the mode of aggregation and directionality of growth. The deposits are constituted from hexagonal platelets as fundamental building blocks, preserving the symmetry of the underlying crystal lattice. Energy minimized Wulff reconstructed surfaces are discernible (Fig. 4C, F, and I), which suggest that the low self-diffusion barriers in this system indeed allow for thermodynamic shapes to be stabilized. However, the mesoscale orientation and attachment of the shapes are highly variable as a function of the concentration and current density. At low concentrations of 0.25 M MeMgCl and high overpotentials, nucleation of new particles dominates over growth of incipient nuclei resulting in fractals comprising aggregates of numerous thin hexagonal platelets on the order of around 3–6 μm in diameter. An increase in concentration of MeMgCl results in a decrease in overpotential and greater availability of ions at reactive sites. Consequently, the growth rates are accelerated and the individual crystallites are substantially larger with a more spherical appearance (with end-to-end dimensions of 30–60 μm , albeit still with some clearly defined hexagonal facets) resulting in a considerably altered

fractal morphology as seen in Fig. 4D–F.⁶⁷ As described below, growth under these conditions corresponds to a diffusion-limited regime; as a result, the observed morphologies are characteristic of diffusion-limited aggregation. At a still higher concentration of 1.0 M MeMgCl, Fig. 3 suggests a notable alteration of the deposition mechanism. SEM images of deposits obtained from 1.5 M THF solutions of MeMgCl (Fig. 4G–I) indicate that increasing concentration brings about a transition from fractal growth to stabilization of dendrites. The deposits exhibit a singular dominant growth tip, albeit with somewhat irregular branches (Fig. 4G–I). Video S4 and Fig. S5 (ESI†) depict lower magnification views of the growth tip (delineated by red arrows in Fig. S5, ESI†). It is worth noting that such growth is distinctly different from the root-growing, needle-like growth observed in lithium.^{48,52} Dendritic growth with the observed dominance of a finite number of growth fronts requires the influence of anisotropy, which may be derived in this case from the intrinsic asymmetry of the hcp crystal structure or, extrinsically, as a result of preferential passivation owing to electrolyte decomposition.^{66,68,69} With diminishing diffusion limitations, the effects of anisotropy are clearly discernible at both the micron- and mesoscale levels.

Thin platelet growth is furthermore observed upon the addition of oleylamine (0.121 M) to the 0.5 M THF solution of MeMgCl at a current density of 0.921 mA cm⁻², as shown in Fig. 6A–C. Oleylamine, a Lewis basic ligand that weakly coordinates to Mg-ions, is thought to buffer the monomer supersaturation and allows for nucleation-dominated growth.^{70,71} Surface passivation necessitates diffusion of monomer ions through the capping layer and likely also alters self-diffusion rates.

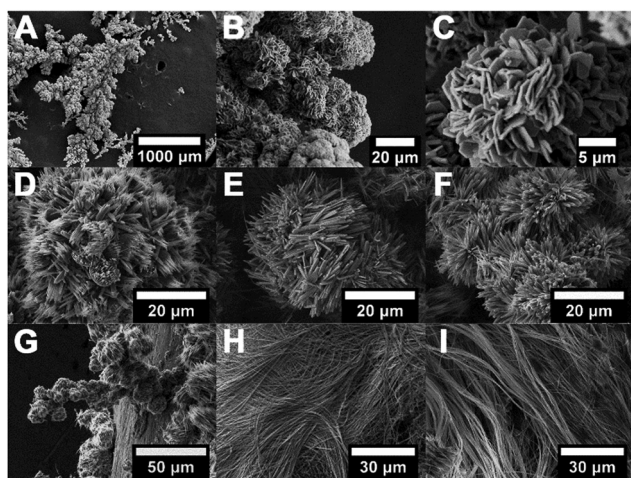


Fig. 6 Ligand modification of Mg Morphologies. SEM images of electro-deposited Mg obtained through addition of (A–C) oleylamine (0.121 M) or (D–I) varying concentrations of dodecanethiol. Spherical clusters of shorter wires have been observed upon addition of (D) 0.0626 M, (E) 0.125 M, and (F) 0.188 M dodecanethiol. These form extended structures as can be observed in (G), which shows a representative example from a reaction containing 0.0626 M dodecanethiol. In addition to clusters, extended 1D wires are observed upon addition of higher concentrations of dodecanethiol as observed upon the addition of (H) 0.125 M and (I) 0.188 M dodecanethiol.

XPS spectra for deposits formed through addition of oleylamine are shown in Fig. S6 (ESI†) and are very similar to that of spectra observed for dendrites formed without the addition of oleylamine with the addition of a characteristic N 1s signal and a shoulder centered around 283.5 eV for the C 1s.

Characterization of Mg dendrites

The microstructure and the growth direction of the Mg dendrites electrodeposited from 1.5 M MeMgCl solutions in THF under 0.921 mA cm⁻² constant current densities have been examined by electron backscatter diffraction (EBSD) and transmission electron microscopy (TEM) (Fig. 5). The dendrites obtained under these conditions span hundreds of microns in width and millimeters in length. Each dendrite comprises a number of Mg crystals with well-defined crystal facets (Fig. 5A). The EBSD and TEM samples have been prepared from an individual branch of a Mg dendrite as shown in Fig. 5B, obtained from the region in Fig. 5A highlighted with the white rectangle; the lengths of the lift-out specimens are parallel to the growth direction of the dendrite. The EBSD map, based on the growth direction of the inverse pole figure (IPF) map and IPF triangular reference, displays a uniform hue, indicating that the examined part of the Mg dendrite is single crystalline. The EBSD map reveals a growth direction of $\langle 11\bar{2}0 \rangle$ (Fig. 5C). The single crystalline nature and growth direction of the Mg dendrites have been further corroborated by TEM observations in Fig. 5D. The corresponding selected area electron diffraction (SAED) pattern (Fig. 5D, inset) confirms the $\langle 11\bar{2}0 \rangle$ growth direction. This growth preference can be rationalized considering that the most dense packing of atoms in hexagonal close-packed Mg is along $\langle 11\bar{2}0 \rangle$.

As seen in Fig. 5E–G, indentation measurements have been used to derive elastic and plastic properties for bulk Mg as well as Mg dendrites electrodeposited from 0.5 and 2 M concentrations of MeMgCl in THF. Indentation of bulk Mg in Fig. 5F yields an elastic modulus of 39.4 ± 0.9 GPa, similar to previously reported values of *ca.* 40–45 GPa in the literature.^{72,73} In contrast, the 0.5 and 2 M electrodeposited Mg deposits exhibit elastic moduli of 23.8 ± 1.6 and 22.5 ± 1.8 GPa, respectively. In other words, the electrodeposited Mg structures possess an elastic modulus nearly 60% that of bulk Mg. Optical observation of the indents (Fig. S7, ESI†) does not reveal excessive pile-up. Furthermore, consistent and flat E^2/H values at substantial depths as well as the frame stiffnesses⁷⁴ favorable comparison with that of the calibration material (fused silica) provides further verification of the validity of these results. Possible origins of the reduced elastic moduli observed for the dendrites include the presence of porosity, impurities in the electrodeposited Mg, and/or the influence of the grain size and orientation of the electrodeposited Mg.

Analysis of plastic properties suggests that the electrodeposition parameters furthermore influence the resulting mechanical properties of the Mg deposits. As seen in Fig. 5G, the indentation of bulk Mg yields a hardness of 665 ± 33 MPa. Assuming a Tabor factor of 2.8, the yield strength of the bulk Mg can be estimated to be ~ 235 MPa.^{73,75,76} At an indentation depth of 1500 nm, the Mg

electrodeposited from 0.5 and 2 M MeMgCl in THF displayed hardness values of 525 ± 38 MPa and 415 ± 18 MPa (corresponding to yield strengths of ~ 190 and 150 MPa), respectively. The origins of the differences in plastic properties from bulk Mg remain unclear but again may be related to impurities (*e.g.*, precipitates) or specifics of the microstructure (*e.g.*, grain sizes, dislocation densities) that form during electrodeposition under different conditions.

A popular model for predicting conditions to prevent dendrite formation is that of Newman and Monroe, who considered electrode stability of electrode (lithium)/separator (or solid electrolyte) interfaces using linear elasticity theory. According to their model, dendrites can be suppressed by a separator or solid electrolyte that has a shear modulus approximately twice that of the electrode itself.⁷⁷ Taking the elastic modulus for the dendritic Mg as 25 GPa and the Poisson's ratio as 0.35,⁷⁸ the shear modulus of a dendrite can be calculated as $\mu = E/[2(1 + \nu)] = 10.0$ GPa. As a result, the Newman and Monroe⁷⁷ model predicts that a separator or solid state electrolyte with a shear modulus of more than ~ 20 GPa will be necessary to prevent the formation of Mg dendrites within a battery. Since polymer separators typically have moduli on the order of 1 GPa and a Poisson's ratio of 0.46,⁷⁹ their shear modulus of ~ 340 MPa is much too small to prevent the propagation of Mg dendrites. However, stiff ceramic solid-state electrolytes with large shear moduli (>25 GPa) may suppress dendrites and thereby warrant further investigation. Notably, both of these electrodeposited Mg morphologies possess significantly larger elastic moduli and hardness values as compared to Li (modulus of ~ 9 GPa and bulk indentation hardness of 4.5 MPa).^{80,81} As a result, mechanically suppressing dendritic growth may prove substantially more challenging than in the case of Li.

Ligand modification of electrodeposition morphologies

The addition of dodecanethiol yields a pronounced change in appearance, a gray powder is obtained at low concentrations of dodecanethiol, whereas an entangled fibrous mat is recovered at high concentrations. Fig. 6D–I show a pronounced modification of the morphology upon the addition of dodecanethiol at different concentrations. Powder XRD patterns for deposits grown with addition of dodecanethiol can be indexed to metallic Mg (PDF 35-0821, Fig. S8, ESI†). XPS spectra of the nanowires formed through the addition of 0.125 M dodecanethiol are shown in Fig. S9 (ESI†) and show similar features to that of the dendrites formed without addition of the alkyl thiol, with the addition of a S 2p band and a shoulder at around 283.5 eV for the C 1s spectrum. An initial reaction between MeMgCl and dodecanethiol produces a thiolate species and MgCl^+ ; as such the dynamics of deposition is substantially altered. Selective adsorption of the thiolate molecules on specific growth facets and the ability of the Lewis basic ligands to buffer the monomer supersaturation substantially reduces the effective monomer flux.^{70,82,83} Under these conditions, the self-diffusion characteristics are comparable to the flux rate; consequently, arrays of faceted nanowires with lateral dimensions of

250–800 nm are observed. Nanowires appear in two primary forms; spherical clusters of shorter wires around 10–20 μm in length are observed upon addition of 0.0626 M, 0.125 M, and 0.188 M dodecanethiol as shown in Fig. 6D–F, respectively. As shown in Fig. 6G, such nanowires furthermore form mesoscale patterns through aggregation of the spheres. Still higher concentrations of dodecanethiol result in the stabilization of long Mg nanowires on the order of many tens to hundreds of micrometers in length (Fig. 6H and I); the nanowires form entangled mats without the higher order aggregation observed at lower dodecanethiol concentrations. This method of achieving the controlled deposition of nanowire arrays furthermore provides a route to nanotextured metallic anode films directly integrated onto the current collector. The results demonstrate the ability to prepare a disparate range of highly textured Mg anode films from electroplating of Grignard's reagents. Cycling of nanowire arrays is expected to yield improved reaction kinetics and a reduced local overpotential owing to the greater availability of deposition sites, thereby reducing the predilection for dendrite formation. The utilization of such anodes in conjunction with dual salt electrolytes portends intriguing battery architectures designed to mitigate dendrite formation.^{27,28}

Plating phase maps and mechanistic underpinnings

The morphology of electrodeposited Mg is governed by the interplay of electrochemistry, ion transport, nucleation, and crystal growth. Specifically, the balance between ion transport in the electrolyte, Mg surface diffusion on the plating electrode, and the electrochemical reaction rate dictate the observed morphologies. At applied current rates, i_{app} (A m^{-2}), exceeding the limiting current density, i_{lim} , for the electrochemical system under observation, diffusional transport in the electrolyte can become the limiting mechanism, resulting in the depletion of Mg^{2+} ions from the proximity of the plating electrode. As such, transformation from smooth to dendritic structures is correlated with this scarcity of Mg^{2+} occurring at Sand's time, τ_{Sand} , given by

$$\tau_{\text{Sand}} = \frac{\pi D(zc_0F)^2}{4(i_{\text{app}}t_a)^2} \Rightarrow D = \frac{4(i_{\text{app}}t_a)^2 \cdot \tau_{\text{Sand}}}{\pi(zc_0F)^2} \quad (1)$$

Here, z is the cationic charge number, c_0 is the bulk salt concentration in the electrolyte (mol m^{-3}), F is Faraday's constant (C mol^{-1}), D is the binary diffusion coefficient ($\text{m}^2 \text{s}^{-1}$) and t_a is the anionic transference number. Determination of Sand's time can help in accurate quantification of electrolyte diffusivity, which is generally a monotonically decreasing function of concentration owing to concentrated solution effects and hence cannot be taken as constant. Further electrodeposition beyond Sand's time results in preferential growth of dendritic structures. For our experiments, the Sand's time parameter values can be directly correlated to the amount of dendritic magnesium, m , tabulated in Table 1 as per Faraday's law:

$$I \cdot (\tau_{\text{total}} - \tau_{\text{Sand}}) = \frac{zFm_{\text{den}}}{M} \quad (2)$$

where I is the applied current (A), τ_{total} is the total temporal duration of the experiment (s), m_{den} is the amount of dendritic magnesium and M is the molar mass of magnesium. Table 1 reports the mass of electroplated dendritic Mg deposits for constant current electroplating at 0.921 mA cm^{-2} over a 24 h total time period for varying electrolyte concentrations. Consequently, equivalent Sand's time can be computed for each of the experimental conditions reported in Table 1. This further enables the estimation of the electrolyte diffusion coefficient, which is required in order to compute the limiting current density.

Limiting current density is estimated from the computed diffusivity as per:

$$i_{\text{lim}} = \frac{2zc_0FD}{t_a L} \quad (3)$$

Here, L is the inter-electrode distance (5.715 cm in the system under consideration). The computed diffusivities and limiting current densities are reported in Table 2, and the corresponding variation with electrolyte concentration is also shown explicitly in Fig. 7B and C. As pointed out earlier, the diffusivity

Table 2 Calculated values for mean diffusivity and limiting current densities for reactions with varying concentrations of MeMgCl in THF based on Sand's time calculations

Concentration (M)	Mean diffusivity ($\text{m}^2 \text{s}^{-1}$)	Mean limiting current density (mA cm^{-2})
0.25	1.43×10^{-9}	0.22
0.5	2.41×10^{-10}	0.05
1.0	1.93×10^{-10}	0.13
1.5	4.95×10^{-11}	0.06
2.0	3.14×10^{-10}	0.07

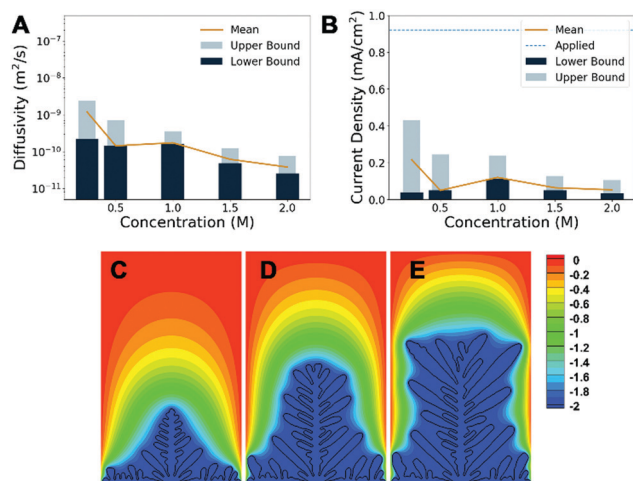


Fig. 7 (A) Variation of diffusion coefficient with bulk electrolyte concentration. Electrolyte diffusivity decreases with concentration. (B) Variation of limiting current density with electrolyte concentration. Limiting current density shows a non-monotonic trend because of the competing effects of electrolyte concentration and electrolyte diffusivity. (C–E) Evolution of dendritic growth from an initial seed located in the bottom center of the domain based on phase field modeling for a dendrite grown in 1 M MeMgCl with three time points representing $t^* = 5$, $t^* = 10$, and $t^* = 15$.

shows a decreasing trend with concentration. However, the limiting current density has a non-monotonic trend owing to the competing effects of increasing salt concentration and decreasing diffusivity. Notably, the regimes evaluated here are consistently above this limiting current density, which enables mapping of non-equilibrium deposition regimes.

It is notable that while the calculations here pertain to global conditions, diffusion limitations can further play an important role in mediating localized heterogeneous deposition. Electrode interfacial inhomogeneities arising from inadequate electrolyte wetting, a heterogeneous solid electrolyte interphase (SEI), and rough electrode surfaces can create localized reaction zones governed by local diffusion considerations. While poor electrolyte wetting is generally a result of electrolyte–electrode mismatch in terms of interfacial wettability or low concentration electrolyte operation, spatial variability of the chemical constituents in a multicomponent SEI can result in a non-uniform Mg-ion flux. Surface perturbations can furthermore serve as preferential deposition sites as a result of the warping of the electric field adjacent to surface protrusions, evidenced by the preferred formation of Mg dendrites near the edges in Fig. 2 and 3. Given that this is an open system, a similar effect is observed with disk electrodes (Fig. S10, ESI[†]) where fields are localized and concentration gradients are amplified at the edges. The subsequent steep increase in local reaction rates can far surpass Mg self-diffusion on the electrode surface.³⁵ In particular, electrolyte diffusion limitations at high currents beget dendritic Mg morphologies with the specific surface diffusion rates dictating fractal-like or needle-like growth regimes as mapped in Fig. 7. The addition of ligand molecules buffers the electrolyte concentration and alters the effective diffusivity, whilst promoting preferential growth morphologies as a result of selective binding to specific facets. Consequently, the dynamic interplay between the electrochemical Damkohler number (Da) contrasting the reaction and self-diffusion rates⁸⁴ and the electrochemical Biot number (Bi) contrasting the reaction and electrolyte transport rates governs the morphologies of electrodeposited Mg stabilized at high current densities.⁸⁵

Further insight into the growth of dendritic structures has been derived from phase-field modeling calculations. The quaternary phase diagram in Fig. S11A (ESI[†]) illustrates the equilibrium relationship between the different components of the system under consideration. A plane is defined to illustrate zero charge conditions and the respective tie lines depict the equilibria varying between Mg(M)–THF at negative electrode potentials and Mg(M)–MeMgCl at positive electrode potentials. MgCl₂ species known to form passivation layers on surfaces of Mg electrodes are further considered.⁸⁶ The dynamical model is initiated by seeding a nucleation event at the electrolyte–electrode surface situated at the bottom center of the domain. Fig. S11B (ESI[†]) shows a dendrite evolved from an initial seed. Fig. 7C–E shows progression of dendrite growth as a function of time. Fig. S11C (ESI[†]) indicates the extracted information from the overview microstructure along the blue arrow. The three extracted curves correspond to the phase-field order

parameter (ζ), Mg^{2+} concentration and electrostatic potential (ψ). The local variations of Mg^{2+} concentration and electrostatic potential at the dendrite tip can be clearly observed in the 1D extracted lines. The overall kinetics of growth are dictated by the energetics of the electrode/electrolyte interface and the Mg^{2+} concentration gradient, which in turn is determined by the surface tension and electrostatic potential. Fig. S11C (ESI[†]) indicates that both concentration and electric potential gradients are larger in the vicinity of the tip, which in turn increases the local overpotential and results in faster growth. Fig. S11D (ESI[†]) depicts the Butler–Volmer kinetics under three different symmetry factors. A value of $\alpha = 0.5$ has been used in this study based on values reported in the literature for analogous Mg electrolyte complexes.⁸⁶ The results indicate that the velocity of the deposition interface follows a highly nonlinear behavior, as is indeed observed in Videos S1–S5 (ESI[†]).

Experimental

Electrodeposition conditions and videomicroscopy

Symmetric cells were assembled in an argon-filled glove box (<0.1 ppm O_2) within three-neck round bottom flasks with two electrode leads run through two of the rubber septa with a separation of 5.715 cm. Both leads held Mg ribbon electrodes (Alfa Aesar, purity of 99.5%) creating symmetric cells. MeMgCl solutions (3 M in anhydrous tetrahydrofuran (THF), Alfa Aesar) were diluted using anhydrous THF (DriSolv, EMD Millipore Co., purity of $\geq 99.9\%$). Ligand effects were evaluated through the addition of oleylamine (0.121 M, Sigma Aldrich) or dodecanethiol (0.0626 M, 0.125 M, or 0.188 M, Sigma Aldrich). Electrodeposition was performed under Schlenk conditions in an Ar atmosphere using a programmable power supply (FB1000, Fisher Scientific) and applying a constant current. A videomicroscope (Plugable Technologies) was used to monitor the reactions.

Structural characterization of deposits

Deposits easily were separated from the Mg substrate through gentle washing with THF. Powder X-ray diffraction (XRD) was performed in Bragg–Brentano geometry using a Bruker D8-Focus diffractometer (Cu $K\alpha$: $\lambda = 1.5418$ Å; 40 kV voltage; 25 mA current). X-ray photoelectron spectra (XPS) were obtained using an Omicron DAR 400 XPS/UPS system with a 128-channel micro-channel plate Argus detector using a Mg $K\alpha$ X-ray source (1253.6 eV). A CN10 electron flood source was utilized to reduce charging. High-resolution scans were collected in constant analyzer energy (CAE) mode with a 100 eV pass energy and a step size of 0.05 eV. Spectral line shapes were fit using the Marquart–Levenberg algorithm for mixed Gaussian–Lorentzian (7:3) line shapes. All spectra were aligned to the C 1s line of adventitious carbon at 284.8 eV.

Electron microscopy

Scanning electron microscopy images were obtained using a JEOL JSM-7500F operating at an accelerating voltage of 10 kV,

emission current of 5 μA , and a probe current of 10 μA . Cross-sectional TEM samples of Mg dendrites were prepared using a FEI Helios Nanolab 460F1 Dual-Focused Ion Beam (FIB). The crystal structure and the growth direction of the Mg dendrites were identified using electron backscatter diffraction (EBSD, Tescan FERA-3 scanning electron microscope (SEM) with an accelerating voltage of 20 kV) and bright-field transmission electron microscopy (TEM, FEI Tecnai G2 F20 Super-Twin FE-TEM operated at 200 kV).

3D X-ray tomography

Soft X-ray microscopy images were recorded at the SM (101D-1) beamline of the Canadian Light Source (CLS). The sample was mounted on a computer-controlled (x , y , θ) tilt-stage, which facilitates spectrotomographic measurements. Tomography data was acquired at the Mg K-edge from $+70^\circ$ to -35° in increments of 5° . Data analysis was performed using TomoJ, a plug-in to the image analysis software, ImageJ.⁸⁷ The images were first aligned using Fourier cross-correlation methods, then further refined using 3D landmarks. In the latter, an algorithm locates regions that can be tracked within the series without the aid of fiducial markers.⁸⁸ Conversion to optical density was carried out using aXis2000 (<http://unicorn.mcmaster.ca/aXis2000.html>). A 3D reconstruction was performed on the aligned tilt-series using an algebraic reconstruction technique (ART), accessible through TomoJ.⁸⁹ A total of 10 iterations were carried out with a relaxation coefficient of 0.08.

Nanomechanical characterization of deposits

Strips of pristine Mg substrate (never used for electrodeposition) as well as the 0.5 and 2 M electrodeposits were cast into separate epoxy stubs. These embedded samples were consecutively mechanically polished using 9, 3, 1, and 0.05 μm diamond suspensions. After polishing, the elastic modulus and hardness of the samples were measured using a Nanomechanics iMicro indenter equipped with an InForce 50 actuator and a diamond Berkovich tip. The standard approach of Oliver and Pharr was used to estimate the elastic modulus and hardness.⁹⁰ Indentation implemented a test with constant $\dot{P}/P = 0.21$ s^{-1} , with continuous stiffness oscillation of 2 nm. Twelve indentation tests were used for each sample as the basis for the reported mechanical measurements.

Model formulation

Electrolyte diffusion limitations. The amount of dendritic magnesium from experiments can be directly correlated to the time between onset of Sand's time limitation and end of experimental runtime. Consequently, the electrolyte diffusion coefficient and symmetric cell system limiting current densities can be evaluated to explain the formation of magnesium dendrites. Cationic transference numbers reported in the literature for EtMgCl in THF, ranging from 0.058 at 0.25 M to 0.018 at 0.4 M, have been used to develop the model.⁹¹ Low mobilities of dimeric species and ion–ion interactions at high concentrations are thought to be the origin of the diminution of the transference number at high concentrations.

Numerical integration of the phase field model. Formulation of the phase field model is described in the ESI.† A metallic Mg electrode in contact with a 1 M MeMgCl solution in THF was selected as the reference state. For the equilibrium numerical simulations, the Mg electrode was located at the bottom of the simulation cell and an artificial nucleation event was introduced. The partial molar volumes of Mg^{2+} , MeMgCl, and THF are approximated to be the same. Eqn (S10)–(S12) (ESI†) were solved using a finite difference solver in a uniform grid with equal mesh size using a parallel in-house Fortran code. Boundary conditions used for eqn (S7)–(S9) are listed in Table S1 (ESI†). Only half of the cell was considered in order to reduce the computational cost; the domain cell size was set at 300×500 .

Conclusions

The promise and excitement of magnesium batteries derives in large portion from the idea that they are immune to dendrite formation. Whilst considerable effort has been invested in the design of novel electrolytes and cathode materials, multivariate studies of Mg electrodeposition are scarce particularly under conditions emulative of high local concentration and potential gradients. Galvanostatic electrodeposition of metallic Mg from Grignard reagents in symmetric cells reveals a complex phase map with varying morphologies of plated deposits including fractal aggregates and highly anisotropic dendrites with singular growth fronts. Based on electron microscopy, X-ray tomography, and optical tomography observations, the deposits are highly faceted primarily zerovalent magnesium with some surface passivation. The growth morphologies have been examined as a function of current density, concentration, and added coordinating ligands. Increase of the current density amplifies the extent of branching, indicating an increase in the electrochemical reaction rate; increases in concentration induce a transition from a fractal to a dendritic growth regime. Remarkably, the dendrites show extended single crystalline domains along the $\langle 11\bar{2}0 \rangle$ growth direction. At lower concentrations, smaller grains comprising agglomerated thin hexagonal platelets are observed. In contrast, at higher concentrations more spherical deposits with faceted hexagonal surficial features are seen. At the highest concentrations, canonical dendritic deposits with a strongly anisotropic growth direction are observed. Addition of coordinating ligands greatly alters the growth mechanisms suppressing dendrite growth and instead stabilizing single-crystalline high-aspect-ratio nanowires by altering the extent of supersaturation and the nature of the electrode/electrolyte interface.

Dendritic electrodeposition is a result of electrolyte transport limitations, with surface self-diffusion rates dictating morphological variation from needle-like to fractal-like morphologies. Synergistic analytical and phase-field modeling further establish the proclivity of Mg to form dendrites at high current densities; variations in electrolyte diffusivity variation with concentrations have further been delineated. Whilst data on long-term cycling performance of Mg full cells is scarce and it remains to be observed the extent to which dendrite formation

will emerge as a limitation, it is worth noting that electrochemical reaction rates can readily surpass self-diffusion rates as a result of local inhomogeneities; as such, the results herein are expected to be relevant to systems even wherein averages current densities are substantially lower. The hardness of Mg dendrites delineated here, with shear moduli approaching 10 GPa, is substantially greater than Li dendrites, and further suggests the need for caution in the design of separators.

Conflicts of interest

There are no conflicts to declare.

Acknowledgements

R. D. acknowledges the Data-Enabled Discovery and Design of Energy Materials program funded under NSF award DGE-1545403. D. S. and C. D. F. would like to acknowledge the support of the National Science Foundation Graduate Research Fellowship under grant No. DGE-1746932 and DGE-1746932 respectively. This work was supported by the National Science Foundation under DMR 1809866. 3D tomography using STXM was performed at the Canadian Light Source, which is supported by the Natural Sciences and Engineering Research Council of Canada, the National Research Council Canada, the Canadian Institutes of Health Research, the Province of Saskatchewan, Western Economic Diversification Canada, and the University of Saskatchewan. Authors also acknowledge the Materials Characterization Facility at Texas A&M for work using SEM and XPS.

References

- 1 N. Nitta, F. Wu, J. T. Lee and G. Yushin, *Mater. Today*, 2015, **18**, 252–264.
- 2 E. A. Olivetti, G. Ceder, G. G. Gaustad and X. Fu, *Joule*, 2017, **1**, 229–243.
- 3 J. W. Choi and D. Aurbach, *Nat. Rev. Mater.*, 2016, **1**, 16013.
- 4 B. Liu, J.-G. Zhang and W. Xu, *Joule*, 2018, **2**, 833–845.
- 5 D. Aurbach, E. Zinigrad, Y. Cohen and H. Teller, *Solid State Ionics*, 2002, **148**, 405–416.
- 6 K. J. Harry, D. T. Hallinan, D. Y. Parkinson, A. A. MacDowell and N. P. Balsara, *Nat. Mater.*, 2014, **13**, 69–73.
- 7 M. Jäckle, K. Helmbrecht, M. Smits, D. Stottmeister and A. Groß, *Energy Environ. Sci.*, 2018, **11**, 3400–3407.
- 8 G. Henkelman, B. P. Uberuaga and H. Jónsson, *J. Chem. Phys.*, 2000, **113**, 9901–9904.
- 9 L. C. Merrill and J. L. Schaefer, *Front. Chem.*, 2019, **7**, 194.
- 10 D. Aurbach, Y. Cohen and M. Moshkovich, *Electrochem. Solid-State Lett.*, 2001, **4**, A113.
- 11 J. O. Besenhard and M. Winter, *ChemPhysChem*, 2002, **3**, 155–159.
- 12 C. B. Bucur, T. Gregory, A. G. Oliver and J. Muldoon, *J. Phys. Chem. Lett.*, 2015, **6**, 3578–3591.
- 13 C. Ling, D. Banerjee and M. Matsui, *Electrochim. Acta*, 2012, **76**, 270–274.

- 14 M. Matsui, *J. Power Sources*, 2011, **196**, 7048–7055.
- 15 J. Muldoon, C. B. Bucur and T. Gregory, *Chem. Rev.*, 2014, **114**, 11683–11720.
- 16 Q. Fu, A. Sarapulova, V. Trouillet, L. Zhu, F. Fauth, S. Mangold, E. Welter, S. Indris, M. Knapp, S. Dsoke, N. Bramnik and H. Ehrenberg, *J. Am. Chem. Soc.*, 2019, **141**, 2305–2315.
- 17 A. Parija, Y. Liang, J. L. Andrews, L. R. De Jesus, D. Prendergast and S. Banerjee, *Chem. Mater.*, 2016, **28**, 5611–5620.
- 18 B. Zhou, H. Shi, R. Cao, X. Zhang and Z. Jiang, *Phys. Chem. Chem. Phys.*, 2014, **16**, 18578–18585.
- 19 E. Levi, Y. Gofer and D. Aurbach, *Chem. Mater.*, 2010, **22**, 860–868.
- 20 H. D. Yoo, Y. Liang, H. Dong, J. Lin, H. Wang, Y. Liu, L. Ma, T. Wu, Y. Li, Q. Ru, Y. Jing, Q. An, W. Zhou, J. Guo, J. Lu, S. T. Pantelides, X. Qian and Y. Yao, *Nat. Commun.*, 2017, **8**, 339.
- 21 D. Aurbach, Y. Gofer, A. Schechter, O. Chusid, H. Gizbar, Y. Cohen, M. Moshkovich and R. Turgeman, *J. Power Sources*, 2001, **97–98**, 269–273.
- 22 J. Muldoon, C. B. Bucur and T. Gregory, *Angew. Chem., Int. Ed.*, 2017, **56**, 12064–12084.
- 23 T. Gao, S. Hou, K. Huynh, F. Wang, N. Eidson, X. Fan, F. Han, C. Luo, M. Mao, X. Li and C. Wang, *ACS Appl. Mater. Interfaces*, 2018, **10**, 14767–14776.
- 24 Q. S. Zhao, Y. N. Nuli, Y. S. Guo, J. Yang and J. L. Wang, *Electrochim. Acta*, 2011, **56**, 6530–6535.
- 25 S. DeWitt, N. Hahn, K. Zavadil and K. Thornton, *J. Electrochem. Soc.*, 2016, **163**, A513–A521.
- 26 M. Jäckle and A. Groß, *J. Chem. Phys.*, 2014, **141**, 174710.
- 27 J. Tian, D. Cao, X. Zhou, J. Hu, M. Huang and C. Li, *ACS Nano*, 2018, **12**, 3424–3435.
- 28 Y. Zhang, J. Xie, Y. Han and C. Li, *Adv. Funct. Mater.*, 2015, **25**, 7300–7308.
- 29 P. G. Shewmon, *Trans. Metall. Soc. AIME*, 1956, **206**, 918–922.
- 30 J. Combronde and G. Brebec, *Acta Metall.*, 1971, **19**, 1393–1399.
- 31 S. Ganeshan, L. G. Hector and Z. K. Liu, *Comput. Mater. Sci.*, 2010, **50**, 301–307.
- 32 L. J. Zhang, T. I. Spiridonova, S. E. Kulkova, R. Yang and Q. M. Hu, *Comput. Mater. Sci.*, 2017, **128**, 236–242.
- 33 A. Parija, G. R. Waetzig, J. L. Andrews and S. Banerjee, *J. Phys. Chem. C*, 2018, **122**, 25709–25728.
- 34 T. D. Gregory, R. J. Hoffman and R. C. Winterton, *J. Electrochem. Soc.*, 1990, **137**, 775–780.
- 35 R. Davidson, A. Verma, D. Santos, F. Hao, C. Fincher, S. Xiang, J. Van Buskirk, K. Xie, M. Pharr, P. P. Mukherjee, S. Banerjee, J. Van Buskirk, K. Xie, M. Pharr, P. P. Mukherjee and S. Banerjee, *ACS Energy Lett.*, 2019, **4**, 375–376.
- 36 J. Bitenc, K. Pirnat, E. Žagar, A. Randon-Vitanova and R. Dominko, *J. Power Sources*, 2019, **430**, 90–94.
- 37 C. Liebenow, *J. Appl. Electrochem.*, 1997, **27**, 221–225.
- 38 M. S. Ding, T. Diemant, R. J. Behm, S. Passerini and G. A. Giffin, *J. Electrochem. Soc.*, 2018, **165**, A1983–A1990.
- 39 H. Brune, *Surf. Sci. Rep.*, 1998, **31**, 125–229.
- 40 J. W. Evans, P. A. Thiel and M. C. Bartelt, *Surf. Sci. Rep.*, 2006, **61**, 1–128.
- 41 A. Groß, *Theoretical Surface Science – A Microscopic Perspective*, Springer, Berlin, 2nd edn, 2009.
- 42 K. Pettersen, O. Lohne and N. Ryum, *Metall. Trans. A*, 1990, **21**, 221–230.
- 43 D. Dubé, A. Couture, Y. Carbonneau, M. Fiset, R. Angers and R. Tremblay, *Int. J. Cast Met. Res.*, 1998, **11**, 139–144.
- 44 K. N. Wood, E. Kazyak, A. F. Chadwick, K. H. Chen, J. G. Zhang, K. Thornton and N. P. Dasgupta, *ACS Cent. Sci.*, 2016, **2**, 790–801.
- 45 K. Nishikawa, T. Mori, T. Nishida, Y. Fukunaka, M. Rosso and T. Homma, *J. Electrochem. Soc.*, 2010, **157**, A1212.
- 46 W.-S. Kim and W.-Y. Yoon, *Electrochim. Acta*, 2004, **50**, 541–545.
- 47 A. J. Ilott, M. Mohammadi, H. J. Chang, C. P. Grey and A. Jerschow, *Proc. Natl. Acad. Sci. U. S. A.*, 2016, **113**, 10779–10784.
- 48 P. Bai, J. Li, F. R. Brushett and M. Z. Bazant, *Energy Environ. Sci.*, 2016, **9**, 3221–3229.
- 49 J. Y. Song, H. H. Lee, Y. Y. Wang and C. C. Wan, *J. Power Sources*, 2002, **111**, 255–267.
- 50 G. Bieker, M. Winter and P. Bieker, *Phys. Chem. Chem. Phys.*, 2015, **8670**, 8670–8679.
- 51 J. C. Burns, L. J. Krause, D.-B. Le, L. D. Jensen, A. J. Smith, D. Xiong and J. R. Dahn, *J. Electrochem. Soc.*, 2011, **158**, A1417.
- 52 F. Hao, A. Verma and P. P. Mukherjee, *ACS Appl. Mater. Interfaces*, 2018, **10**, 26320–26327.
- 53 L. Viyannalage, V. Lee, R. V. Dennis, D. Kapoor, C. D. Haines and S. Banerjee, *Chem. Commun.*, 2012, **48**, 5169.
- 54 D. Aurbach, *Electrochem. Solid-State Lett.*, 1999, **3**, 31.
- 55 C. Fotea, J. Callaway and M. R. Alexander, *Surf. Interface Anal.*, 2006, **38**, 1363–1371.
- 56 H. Kuwata, M. Matsui and N. Imanishi, *J. Electrochem. Soc.*, 2017, **164**, A3229–A3236.
- 57 Y. Gofer, R. Turgeman, H. Cohen and D. Aurbach, *Langmuir*, 2003, **19**, 2344–2348.
- 58 R. M. Bradley and R. C. Ball, *Nature*, 1984, **309**, 225–229.
- 59 V. Fleury, M. Rosso, J.-N. N. Chazalviel and B. Sapoval, *Phys. Rev. A: At., Mol., Opt. Phys.*, 1991, **44**, 6693–6705.
- 60 Y. Sawada, A. Dougherty and J. P. Gollub, *Phys. Rev. Lett.*, 1986, **56**, 1260–1263.
- 61 D. Grier, E. Ben-Jacob, R. Clarke and L. M. Sander, *Phys. Rev. Lett.*, 1986, **56**, 1264–1267.
- 62 R. F. Voss, *Phys. Rev. B: Condens. Matter Mater. Phys.*, 1984, **30**, 334–337.
- 63 P. Meakin, *Phys. Rev. Lett.*, 1983, **51**, 1119–1122.
- 64 A. Ghosh, R. Batabyal, G. P. Das and B. N. Dev, *AIP Adv.*, 2016, **6**, 015301.
- 65 L. O. Valöen and J. N. Reimers, *J. Electrochem. Soc.*, 2005, **152**, A882.
- 66 D. P. Barkey, *Advances in Electrochemical Science and Engineering*, Wiley-VCH Verlag GmbH, Weinheim, FRG, 2001, vol. 7, pp. 151–191.
- 67 O. Zik and E. Moses, *Phys. Rev. E: Stat. Phys., Plasmas, Fluids, Relat. Interdiscip. Top.*, 1996, **53**, 1760–1764.
- 68 E. Ben-Jacob and P. Garik, *Nature*, 1990, **343**, 523–530.
- 69 W. Shao and G. Zangari, *J. Phys. Chem. C*, 2009, **113**, 10097–10102.

- 70 K. R. Kort and S. Banerjee, *Small*, 2015, **11**, 329–334.
- 71 J. Cho, H. Jin, D. G. Sellers, F. David Watson, D. Hee Son and S. Banerjee, *J. Mater. Chem. C*, 2017, **5**, 8810.
- 72 M. P. Staiger, A. M. Pietak, J. Huadmai and G. Dias, *Biomaterials*, 2006, **27**, 1728–1734.
- 73 *ASM specialty handbook: magnesium and magnesium alloys*, ed. M. Avedesian and H. Baker, ASM International, 1999.
- 74 W. C. Oliver and G. M. Pharr, *J. Mater. Res.*, 2004, **19**, 3–20.
- 75 M. Rashad, F. Pan, A. Tang, M. Asif and M. Aamir, *J. Alloys Compd.*, 2014, **603**, 111–118.
- 76 E. Mostaed, M. Vedani, M. Hashempour and M. Bestetti, *Biomatter*, 2014, **4**, e28283.
- 77 C. Monroe and J. Newman, *J. Electrochem. Soc.*, 2005, **152**, A396–A404.
- 78 *Metals Handbook Desk Edition*, ed. J. R. Davis, Materials Park, OH, 2nd edn, 2003.
- 79 C. T. Love, *J. Electrochem. Energy Convers. Storage*, 2016, **13**, 031004.
- 80 W. S. LePage, Y. Chen, E. Kazyak, K.-H. Chen, A. J. Sanchez, A. Poli, E. M. Arruda, M. D. Thouless and N. P. Dasgupta, *J. Electrochem. Soc.*, 2019, **166**, A89–A97.
- 81 A. Masias, N. Felten, R. Garcia-Mendez, J. Wolfenstine and J. Sakamoto, *J. Mater. Sci.*, 2019, **54**, 2585–2600.
- 82 A. Puzder, A. J. Williamson, N. Zaitseva, G. Galli, L. Manna and A. P. Alivisatos, *Nano Lett.*, 2004, **4**, 2361–2365.
- 83 S. A. Morin, M. J. Bierman, J. Tong and S. Jin, *Science*, 2010, **328**, 476–480.
- 84 F. Hao, A. Verma and P. P. Mukherjee, *ACS Appl. Mater. Interfaces*, 2018, **10**, 26320–26327.
- 85 F. Hao, A. Verma and P. P. Mukherjee, *Energy Storage Mater.*, 2019, **20**, 1–6.
- 86 Y. Viestfrid, M. D. Levi, Y. Gofer and D. Aurbach, *J. Electroanal. Chem.*, 2005, **576**, 183–195.
- 87 C. Messaoudi, T. Boudier, C. Sorzano and S. Marco, *BMC Bioinf.*, 2007, **8**, 288.
- 88 C. Sorzano, C. Messaoudi, M. Eibauer, J. Bilbao-Castro, R. Hegerl, S. Nickell, S. Marco and J. Carazo, *BMC Bioinf.*, 2009, **10**, 124.
- 89 G. T. Herman, A. Lent and S. W. Rowland, *J. Theor. Biol.*, 1973, **42**, 1–32.
- 90 W. C. Oliver and G. M. Pharr, *J. Mater. Res.*, 1992, **7**, 1564–1583.
- 91 A. Benmayza, M. Ramanathan, T. S. Arthur, M. Matsui, F. Mizuno, J. Guo, P.-A. Glans and J. Prakash, *J. Phys. Chem. C*, 2013, **117**, 26881–26888.